31st Annual International Conference of the IEEE EMBS
Minneapolis, Minnesota, USA, September 2-6, 2009

Longitudinal Strain Estimation in Incompressible Cylindrical Tissues from Magnetic Resonance Imaging

Qi Wei and Dinesh K. Pai

Abstract— **In this paper, we present a simple approach for estimating the average longitudinal strains from models reconstructed from medical images. It can be used for many incompressible generalized cylindrical tissues, such as tendons, ligaments, and fusiform muscles; the major deformation directions of these soft tissues are along the longitudinal axes. The method is especially useful when pre- and post-deformation tissue correspondences are difficult to establish directly from images for various reasons, such as insufficient image resolution, homogenous image intensity, and noise. Incompressibility, which is accepted as a good approximation for soft tissues, is exploited as a constraint on the tissue deformation. Experiments with Magnetic Resonance Imaging (MRI) of tissue phantoms and computer simulations show that the method is accurate and practical even in the presence of noise. Finally, we demonstrate the usefulness of our approach on studying extraocular muscle deformation.**

I. INTRODUCTION

Determining deformation properties of soft tissues is a fundamental problem in biomechanics. Realistic biomechanical modeling and simulation requires both reconstruction of anatomical structures and estimation of deformation. For instance, in modeling the mechanics of extraocular muscles, we need to estimate the shortening of the muscles from MR images acquired in multiple gazes, even though the image resolution is not sufficient to identify point correspondences between images. However, accurate and efficient deformation estimation *in vivo* is challenging due to many reasons.

Different imaging modalities have been employed for estimating material properties by tracking tissue deformation; we list a few representatives here. Ultrasound has been used widely for measuring strains [1], [2], because of its noninvasive feature and real time capability. In particular, ultrasound elastography has been developed to measure the tissue elasticities, leading to important applications including lesion detection in breasts and prostates. MRI [3] and fluoroscopic imaging [4] have also been used for strain estimation. Most of these approaches compute the material displacement by finding tissue correspondences in two images. However, it is not always possible to establish correspondences due to poor data resolution, homogeneous intensity across the material, smooth shape deformation, etc.

One approach to solve the correspondence problem is the MRI tagging technique, which introduces tags in the imaging process to capture the underlying tissue movement. Tagged MRI has been used to estimate myocardial strains [5], [6], hamstring strains [7], and extraocular muscle deformation [8]. Magnetic Resonance Elastography (MRE) combines MRI with low-frequency sound waves and is able to measure tissue viscoelasticity [9], [10], [11]. Cine phase-contrast MRI has also been proven to be effective in tracking skeletal muscle motion [12], [13]. Applications using these techniques are limited by their availability and time efficiency. They are mostly restricted to two dimensional strains, assuming that there is no off-plane tissue deformation.

Another way is to introduce physical markers that are easier to track. Dye lines of elastin stain were applied on the gastrocnemius tendon-muscle unit for measuring longitudinal strain [14]. Markers have been attached to the surfaces of tendon and muscle [15], [16], [4] or implanted in extraocular muscles [17]. The surface markers are limited to the study of cadaver tissues or superficial live tissues. The bead implant cannot be used on human subjects.

We propose a simple but effective algorithm for measuring the longitudinal strain of an object when the images are inadequate for providing enough information for the object interior. Usually the boundaries are relatively easy to extract because of the contrast between different tissues. Our goal is to compute the average 1D strain field along the major deformation axis, given only the tissue boundaries of generalized cylindrical shape. A generalized cylinder (GC) is a cylindrical object resulting from sweeping a possibly varying cross section along an arbitrary space curve [18]. It does not have to be axisymmetric since the cross sections can be arbitrary too, which makes GC a flexible and realistic geometric representation of muscles and tendons.

We focus on the longitudinal strain, which is one of the most important parameters in measuring material properties of ligaments and tendons [14], [16], [4]. The key point of our method is that most soft tissues are incompressible to a very good approximation [1], [15], [19]. In other words, the volume of the tissue material is nearly constant in different deformed configurations. By using this physical property, we can compute longitudinal strains by finding subvolume-to-subvolume correspondences instead of discrete point-to-point correspondences.

In Section II, we first introduce our methodology by using a 2D synthetic example for the simplicity of conveying the idea. The approach is directly applicable to three-dimensions. To validate the effectiveness of the approach, we apply it to real MR images of a rubber tissue phantom modeling tendon (see Section III-A). Predicted longitudinal deformation is

Qi Wei is with the Department of Computer Science, University of British Columbia, 2366 Main Mall, Vancouver, BC V6T1Z4, Canada *and* Department of Computer Science, Rutgers University, 110 Frenlinghuysen Road, Piscataway, NJ 08854, USA

Dinesh K. Pai is with the Department of Computer Science, University of British Columbia, 2366 Main Mall, Vancouver, BC V6T1Z4, Canada pai@cs.ubc.ca

978-1-4244-3296-7/09/$25.00 ©2009 IEEE

compared with the ground truth given by the markers inside the phantom. Further evaluation is performed by sensitivity analysis of simulated data in Section III-B. Finally, we show the application of our method on extraocular muscles(see Section III-C).

II. METHODS

For ease of illustration, we describe our algorithm using a simulated 2D muscle-like elastic object. The method applies directly to any generalized cylinder; we demonstrate the method with 3D MRI data in Section III-A.

Figure 1(a) shows a 2D object in the steady state (in red) and its deformed shape (in blue). The deformed boundary is a scaled version of the reflection of its steady shape in the x direction. This simple setup guarantees that the total volume is preserved. Given only the boundaries, we will show how our algorithm computes the strain field along the x-axis. In general, the boundary does not have to be as smooth as this example and the axis can be curved (see Section III).

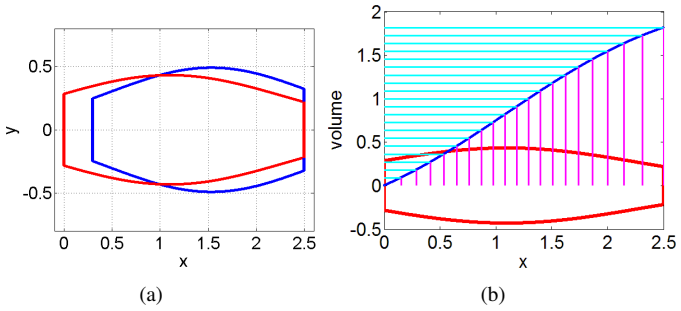

Fig. 1. (a) A 2D example showing an object before and after deformation. (b) The cumulative volume function and the segments from projection.

The whole area (volume) is discretized into equal area (volume) segments along the x-axis. The cumulative volume function over x (shown as a blue curve in Figure 1(b)) is first computed. A finite difference approximation is used to calculate the volume,

$$V_{total} = \sum_{i=1}^{N-1} (x_{i+1} - x_i)(l_{i+1} + l_i)/2, \qquad (1)$$

where l_i is the length (area in 3D) of the vertical section at $x = x_i$ and N is the number of samples. Then the total volume along the vertical volume-axis is uniformly divided (shown as the cyan line segments in Figure 1(b)). The magenta lines in Figure 2(a)) show the projection of equal volume partitions of the x-volume function onto the x-axis. The accuracy of the uniform partition depends on the number of segments. Figure 2(a) shows the 20 segments before and after deformation.

All segments have approximately the same volume, $\Delta V_{before} = \Delta V_{after} = V_{total}/20$. Under the assumption of uniform stress and strain on the cross sections, each volume before deformation can be associated with one afterwards, following the sequential order along the x-axis. Instead of tracking point-to-point correspondences, 1D volume-to-volume correspondences are established using incompressibility. Figure 2(a) shows the segments and their correspondences.

The longitudinal strain of each subvolume is computed as

$$s^i = \frac{\widehat{w^i} - w^i}{w^i}, \qquad (2)$$

where w^i and $\widehat{w^i}$ are the weighted average widths of the i^{th} subvolume before and after deformation. Figure 2(b) shows the estimated strain of the above example. The green curve is the spline interpolation of the raw strain field computed at the centers of the segments (shown as yellow markers).

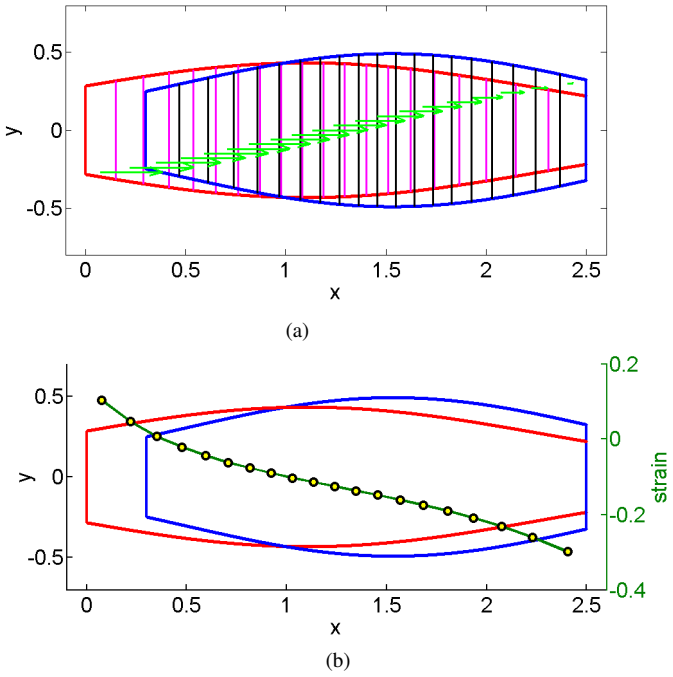

Fig. 2. (a) 20 segments are computed for each state. Volume correspondences are shown by the green displacement arrows between the centers of two corresponding subvolumes. (b) Estimated longitudinal strains are shown as the green curve.

III. RESULTS

We evaluate our method using both real MR image data from a 3D tissue phantom (Section III-A), and computer simulation or sensitivity analysis (Section III-B). We then demonstrate the application of the approach on estimating deformation of extraocular muscles (EOMs) in Section III-C.

A. 3D Phantom Validation

In order to test the applicability of this approach in real applications, evaluation is first performed on real MR images of a rubber phantom mimicking generalized cylindrical soft tissues. MR imaging was used since it is widely used for imaging human subjects *in vivo*.

1) Experiment Design: The tissue phantoms were made from silicone rubber (Smooth-On, Easton, PA) embedded with glass beads (BioSpec, Bartlesville, OK). MR images of the phantoms at different stretched states were acquired from

a Philips 3.0 Tesla MRI scanner. We compare the results of our algorithm to the ground truth obtained by tracking the displacement of the glass beads.

Figure 3(a) shows two rubber phantoms glued to two fiber glass boards in a MR compatible box, viewed from the top. The box stabilizes the phantoms in different stretching states. At the rest state, each phantom is about $83.5mm(L) \times 25mm(W) \times 18mm(H)$. The upper phantom is made of silicone rubber Ecoflex^{TM} with hardness 00-30A and the lower one is from Dragon Skin^{TM} with Shore durometer hardness 10A. About 40 solid glass beads ($1mm$ in diameter) were scattered inside the phantom. The beads appear dark in the images due to their MRI invisibility, while Silicone rubbers appear bright. Such nice contrast enables easy tracking of the bead locations.

2) Experiment Results: T1 weighted gradient echo 3D MR images were acquired from a Philips Achieva 3.0 Tesla MRI scanner in the MRI Research Centre in the University of British Columbia. The scan matrix is 400×200 and the voxel size of the isotropic 3D image data is $0.5mm$. 60 coronal images were scanned in each elongation state. Figure 3 shows pictures of the phantoms at different elongation states as well as the corresponding MR images. The amount of each elongation was determined by the spacing of the vertical slots that supported the phantom. In the rest of the paper, we will mainly discuss the results from the Ecoflex^{TM} phantom due to space limit. From our data analysis, Dragon Skin^{TM} performs similarly to Ecoflex^{TM}.

A threshold segmentation is applied to the reconstructed axial images (thickness $0.5mm$); the cross sectional areas are estimated from the segmented areas. The most stretched state has the maximal volume loss (about 1.22%) compared to the reference state, which is negligible. The approximate volume preservation assumption holds for the phantom.

Glass beads embedded in the phantoms are identified and their centers of mass are used as their 3D locations. Our approach is first validated by computing the error between the predicted marker location and the actual location. Figure 4 plots the errors of all the markers in three elongation states. Notice that the errors are all bounded by the scan resolution $0.5mm$, which proves the accuracy of the method.

We also compare the estimated longitudinal strain of the rubber phantom to the actual strain interpolated from the measured marker displacements. We use the markers that are at least $2mm$ apart in the rest state such that errors due to imaging resolution and marker size can be minimized. Figure 5 shows the strain comparison in three elongated configurations. Our estimated strains well approximate the true strains.

B. Simulated Sensitivity Analysis

In the sensitivity analysis, the input is perturbed by either adding errors to the boundary measurement or violating the basic assumptions by a small amount. The method described in Section II is applied on the perturbed input and errors are analyzed with respect to the noise.

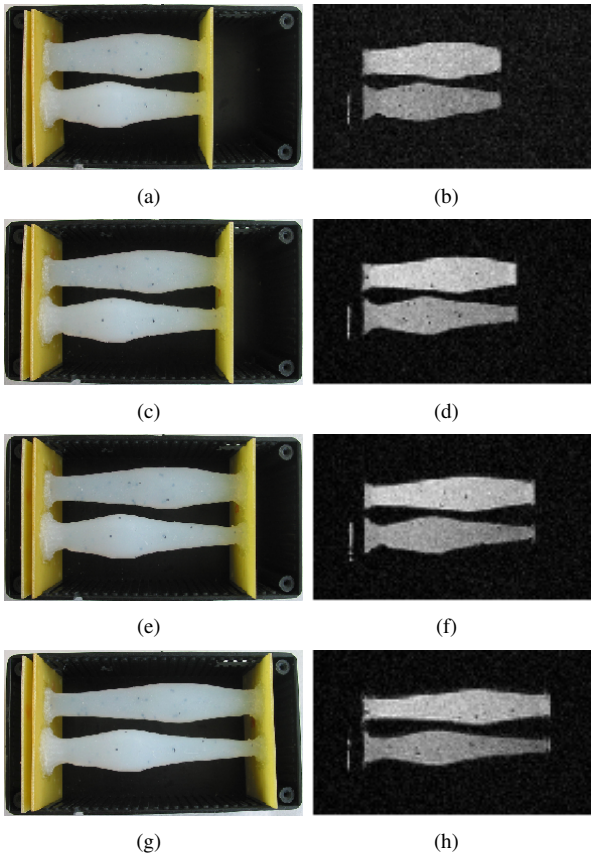

Fig. 3. Photos and the corresponding MR images of the phantoms that were (a)(b) at the reference state; (c)(d) elongated by 1.11; (e)(f) elongated by 1.22; (g)(h) elongated by 1.33. The dimensions of the box are $135mm(L) \times 75(W) \times 70(H)$. The lengths of the phantom in the four configurations are $83.5mm$, $92.7mm$, $101.6mm$, and $111.2mm$ respectively.

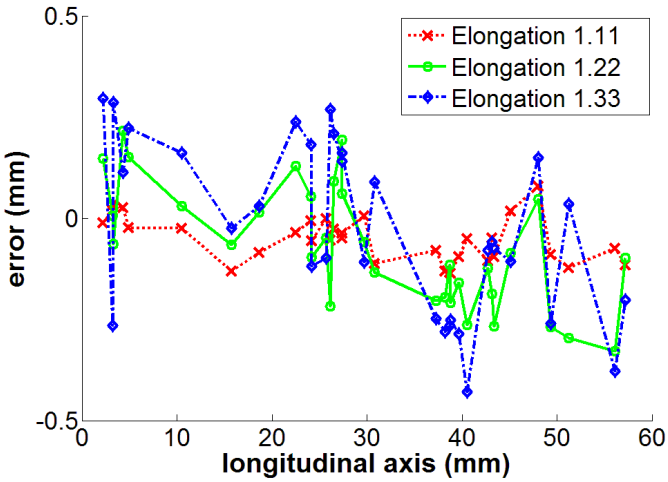

Fig. 4. (a) Absolute axial displacement error in three elongation configurations.

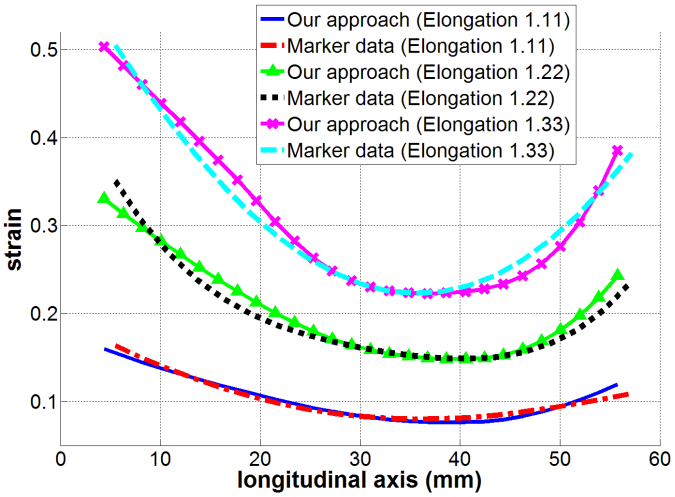

Fig. 5. Comparison of strains estimated from our approach and interpolated from actual marker displacements.

1) Shearing: In this experiment, we assume that the tissue shears to some extent (see Figure 6 for an example). A simple 2D shearing model is considered. Mathematically, each point (x, y) in the object moves to (x', y'), where $x' = x + y \tan \alpha, y' = y$. α is the shear angle.

Obviously, volume is preserved. Both the x-strain and y-strain are zero. If we apply our method, we will not get exactly zero strain along the x-axis because of the geometric distortion perpendicular to the x-axis. Figure 6 shows the estimated strain from an example with 20 degree shearing.

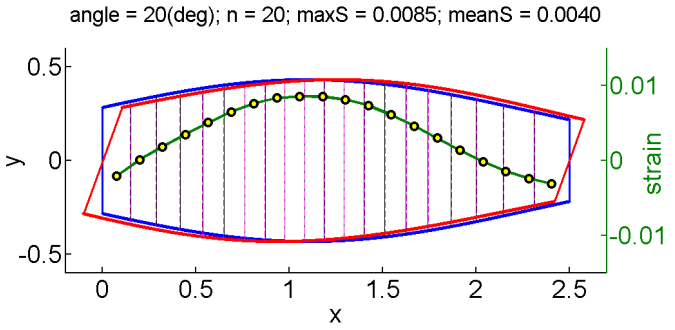

Fig. 6. Original tissue in blue is sheared by 20 degrees and becomes the object in red. Estimated strains are shown as the green curve. Note that the maximum strain is very small (less than 0.01); the vertical scale is magnified to make the small variation in strain visible.

Strain fields at different shearing angles are computed. The magnitude of the strain error is studied, which is just the absolute value of the estimated strain because $|s^i - s_0^i| = |s^i - 0| = |s^i|$, where s^i is the strain of the i^{th} subvolume and s_0^i is the true longitudinal strain under shear. Figure 7 shows the error statistics $max(|s^i|)$ and $average(|s^i|)$ at 20 different shearing angles. As expected, the strain error increases with the shearing angles. The maximum error is only about 0.015, even with shearing of 26 degrees.

2) Additive Gaussian noise: Next, we consider the cases in which the boundary measurement is imperfect. Here the

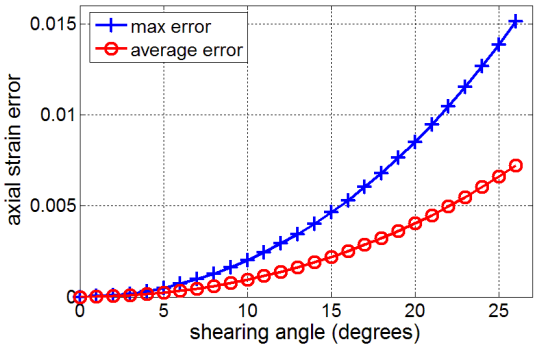

Fig. 7. The statistics of strain errors given different shearing angles.

boundary is assumed to be corrupted by additive Gaussian noise. Thirteen noise levels are tested. For every level, the following process is repeated 100 times and the average is taken as the error measurement. Random Gaussian noise is generated and added to the ground truth. Then the strain fields, s_0 from the original data and s from the noisy data, are estimated respectively. The maximum and average of the strain error magnitude, $max(|s^i - s_0^i|)$ and $average(|s^i - s_0^i|)$, are studied.

Figure 8 shows the statistics of the strain error. The error increases almost linearly with the noise variance. Even with the largest perturbation, the maximum error is still below 0.01. We conclude that our approach is robust against this kind of additive noise.

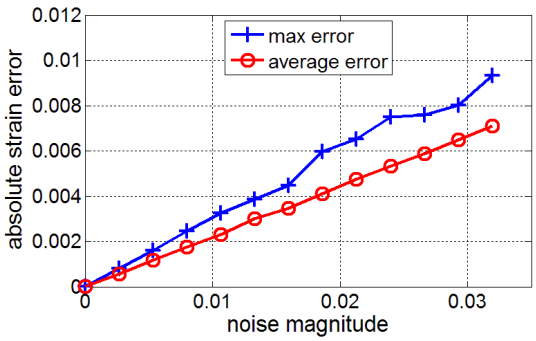

Fig. 8. The maximum and average strain errors given different Gaussian noise variances.

C. Deformation of Extraocular Muscles from MRI

Understanding how the extraocular muscles (EOMs) deform *in vivo* as a function of gaze is important in studying the physiological and mechanical properties of the oculomotor plant. However, measuring EOM deformation is challenging. Miller et al. [17] implanted gold beads in the orbits of monkeys and tracked these markers using CT imaging. Clearly, this technique cannot be used on human subjects. Motion-encoded MRI has recently been used to assess EOM motion [8]. However, limited by the imaging resolution and imaging dimensions, local deformation along the EOM axis has not been available [8]. Our method solves this problem by computing longitudinal strains from models reconstructed

from MRI instead of from images themselves. We see our approach as complementary to the above techniques because of its simplicity and usefulness on widely available conventional MRI from human subjects.

Applying the method described above, we estimated the longitudinal strains of the horizontal EOMs in adduction and abduction using models reconstructed from MR images of human subjects. The calculated strains were applied to generate realistic EOM models in a physically consistent registration framework. Constrained by the estimated EOM deformation, the resulting models are more anatomically accurate and physically meaningful. Details can be found in [21].

IV. Discussion

We present a simple and effective method for estimating longitudinal strains in musculotendons and other generalized cylinders, in cases where local correspondences are hard to find. The underlying idea is to find subvolume-to-subvolume correspondences utilizing the incompressibility of soft tissues. This approach is very practical because shapes of soft tissues can be obtained either from medical images or recently developed laser reflectance system for measuring cross sections [22].

Simulated sensitivity analysis shows that with moderate noise, the algorithm produces small errors. Validation on MRI of a rubber phantom further proves the accuracy of our approach. The method has been applied in studying extraocular muscle deformation.

The proposed method is limited to one-dimensional longitudinal strains and lumped in the transverse directions. It is designed for tendons, ligaments, and fusiform muscles, such as the biceps brachii and extraocular muscles, in which fibers are arranged nearly parallel to each other. It cannot accurately predict strains from muscles with more complex architectures. In future work, we plan to estimate strains from more general deformation with shearing and non-homogeneous tissue properties. If few sparse correspondences are available, we would also like to exploit the incompressibility constraint to deal with more complex structures.

V. ACKNOWLEDGMENTS

We would like to thank Sang Hoon Yeo and Shinjiro Sueda for their help on making the phantoms and useful discussion, Trudy Harris, Dr. Burkhard Mädler, and Dr. Alex MacKay in the UBC MRI Research Centre for the MRI technical support. This research was supported in part by a Canada Research Chair, NSERC, Peter Wall Institute for Advanced Studies, and NIH grant R01NS050942.

References

[1] M.A. Lubinski, S.Y. Emelianov, K.R. Raghavan, A.E. Yagle, A.R. Skovoroda, and M. O'Donnell, Lateral Displacement Estimation Using Tissue Incompressibility, *IEEE Transactions on Ultrasonics, Ferroelectrics, and Frequency Control*, Vol. 43(2), pp 247-256, 1996.

[2] R.S. Witte, K. Kim, B.J. Martin, and M. O'Donnell, Effect of Fatigue on Muscle Elasticity in the Human Forearm Using Ultrasound Strain Imaging, *Proceedings of the 28th Annual International Conference of the IEEE Engineering in Medicine and Biology Society*, pp 4490-4493, 2006.

[3] C.L. Gilchrist, J. Q. Xia, L.A. Setton, and E.W. Hsu, High-Resolution Determination of Soft Tissue Deformations Using MRI and First-Order Texture Correlation, *IEEE Transactions on Medical Imaging*, Vol. 23(5), pp 546-553, 2004.

[4] L.E. DeFrate, A. van der Ven, P.J. Boyer, T.J. Gill, and G. Li, The Measurement of the Variation in the Surface Strains of Achilles Tendon Grafts Using Imaging Techniques. *Journal of Biomechanics*, Vol. 39, pp 399-405, 2006.

[5] N.F. Osman, W.S. Kerwin, E.R. McVeigh, and J.L Prince, Cardiac Motion Tracking Using Cine Harmonic Phase (HARP) Magnetic Resonance Imaging, *Journal of Magnetic Resonance Imaging*, Vol. 42(6), pp 1048-1060, 1999.

[6] N. Reichek, MRI Myocardial Tagging, *Journal of Magnetic Resonance Imaging*, Vol. 10(5), pp 609-616, 1999.

[7] N. Fiorentino, J. Lin, M. Guttman, A. Derbyshire, D. Mazilu, N. Evoy, E. McVeigh, and S.S. Blemker, Characterizing Hamstrings Muscle Dynamics During Knee Flexion-Extension Using Real-Time MRI, *American Society of Biomechanics Annual Conference*, 2007.

[8] M. Piccirelli, R. Luechinger, A.K. Rutz, P. Boesiger, and O. Bergamin, Extraocular Muscle Deformation Assessed by Motion-encoded MRI During Eye Movement in Healthy Subjects, *Journal of Vision*, Vol. 7(14), pp 1-10, 2007.

[9] R. Muthupillai, and R.L. Ehman, Magnetic Resonance Elastography, *Nature Medicine*, Vol. 2, pp 601-603, 1996.

[10] M.A. Dresner, G.H. Rose, P.J. Rossman, R. Muthupillai, A. Manduca, and R.L. Ehman, Magnetic Resonance Elastography of Skeletal Muscle, *Journal Of Magnetic Resonance Imaging*, Vol. 13, pp 269-276, 2001

[11] S.F. Bensamoun, S.I. Ringleb, Q. Chen, R.L. Ehman, K.N. An, and M. Brennan, Thigh Muscle Stiffness Assessed With Magnetic Resonance Elastography in Hyperthyroid Patients Before and After Medical Treatment, *Journal of Magnetic Resonance Imaging*, Vol. 26(3), pp 708-713, 2007.

[12] D.S. Asakawa, G.P. Pappas, S.S. Blemker, J.E. Drace, and S.L. Delp, Cine Phase-Contrast Magnetic Resonance Imaging As a Tool for Quantification Of Skeletal Muscle Motion, *Seminars in Musculoskeletal Radiology*, Vol. 7(4), pp 287-295, 2003.

[13] X. Zhong, F.H. Epstein, B.S. Spottiswelde, P.A. Helm, and S.S. Blemker, Imaging Two-Dimensional Displacements and Strains in Skeletal Muscle During Joint Motion By Cine DENSE MR, *Journal of Biomechanics*, Vol. 41, pp 532-540, 2008.

[14] C.L. Trestik, and R.L. Lieber, Relationship Between Achilles Tendon Mechanical Properties and Gastrocnemius Muscle Function, *Journal of Biomechanical Engineering*, Vol. 115(3), 225-230.

[15] C.C. van Donkelaar, P.J.B. Willems, A.M.M. Muijtjens, and M.R. Drost, Skeletal Muscle Transverse Strain During Isometric Contraction at Different Lengths, *Journal of Biomechanics*, Vol. 32, pp 755-762, 1999.

[16] T.A. Wren, S.A. Yerby, G.S. Beaupre, and D.R. Carter, Mechanical Properties Of the Human Achilles Tendon, *Clinical Biomechanics*, Vol. 16(3), pp 245-251, 2001.

[17] J.M. Miller, E.A. Rossi, M. Wiesmair, D.E. Alexander, and O. Gallo, Stability Of Gold Bead Tissue Markers, *Journal of Vision*, Vol. 6(5), pp 616-624, 2006.

[18] T. O'Donnell, T.E. Boult, X. Fang, and A. Gupta, The Extruded Generalized Cylinder: A Deformable Model For Objectrecovery, *Proceedings of IEEE Computer Society of Computer Vision and Pattern Recognition (CVPR'94)*, pp 174-181, 1994.

[19] M. Epstein, M. Wong, and W. Herzog, Should Tendon and Aponeurosis Be Considered in Series?, *Journal of Biomechanics*, Vol. 39, pp 2020-2025, 2006.

[20] G.P. Pappas, D.S. Asakawa, S.L. Delp, F.E. Zajac, and J. E. Drace, Nonuniform Shortening in the Biceps Brachii During Elbow Flexion, *Journal of Applied Physiology*, Vol. 92, pp 2381-2389, 2002.

[21] Q. Wei, and D.K. Pai, Physically Consistent Registration of Extraocular Muscle Models From MRI, *Proceedings of 30th Annual International Conference of the IEEE Engineering in Medicine and Biology Society*, pp 2237-2241, 2008.

[22] G. Pokhai, K. Gordon, and M. Oliver, Development of a Laser Reflectance System to Measure the Cross-Sectional Area of Soft Tissue, *Meeting of North American Congress on Biomechanics*, 2008.